RSC Advances

ROYAL SOCIETY OF CHEMISTRY

PAPER

View Article Online
View Journal | View Issue

Check for updates

Cite this: *RSC Adv.*, 2023, **13**, 32457

AgBr nanoparticle surface modified SnO_2 enhanced visible light catalytic performance: characterization, mechanism and kinetics study

Hengcan Dai, *[a] Xiaoliang Yang,[b] WanLi Li[c] and Yukai Wang[a]

Received 23rd August 2023
Accepted 23rd October 2023

DOI: 10.1039/d3ra05750j

rsc.li/rsc-advances

In this study, a simple hydrothermal procedure and *in situ* precipitation method were used to prepare SnO_2–AgBr composites, where the molar ratios of SnO_2 and AgBr were 1 : 1, 1 : 2 and 2 : 1. Characterization results showed that the composites had excellent dispersion, crystallinity, and purity. A photocatalytic degradation experiment and first-order kinetic model indicate that SnO_2–AgBr (1 : 1) had the best photocatalytic performance, and the degradation rates of 30 mg L^{-1} simulated MO and MG wastewater reached 96.71% and 93.36%, respectively, in 150 min, which were 3.5 times those of SnO_2. The degradation rate of MO and MG increases with the dosage. Humic acid inhibited the degradation of MG, while a low concentration of humic acid promoted the degradation of MO, and the composite has good stability with pH. A free radical trapping experiment shows that $\cdot OH$ and $\cdot O_2^-$ were the main active substances, and h^+ was the secondary one. According to the results of the characterization and photocatalysis experiments, a Z-scheme mechanism for the SnO_2–AgBr composite was proposed, and the degradation pathway of target pollutants was speculated upon. This study has conceived novel methods for the development of a mature Z-scheme mechanism and in doing so has provided new approaches for the development of photocatalysis for water pollution control.

1. Introduction

With the rapid development of society and the economy, the world produces about 800 000 tons of synthetic dyes every year, of which about 10–15% are transferred to the natural environment by human activities[1,2] This pollutant will not only cause serious pollution to the water environment, affecting the growth metabolism of aquatic creatures, but is also a potential threat to human health.[3–6] Numerous studies have focused on degradation methods for synthetic dyes, such as adsorption,[7] microbial degradation,[8] Fenton reaction,[9] photocatalysis,[10] and electrochemistry.[11] Photocatalytic technology as a green sustainable method that uses solar energy to solve the problem of environmental pollution has received widespread attention due to its low cost and environmentally friendly processing. The strong oxygen reducing active substance produced by the photocatalyst in sunlight can degrade pollutants into intermediate products that are prone to biodegradation in a short period of time, or directly mineralized into H_2O and CO_2.[12–15]

Tin dioxide (SnO_2) is a typical semiconductor material, which has the advantages of non-toxicity, excellent photoelectric performance and low cost, but because of its wide band gap (3.6 eV), it has almost no response to visible light, which greatly limits its application as a photocatalytic material.[16,17] Elemental mixing and semiconductor compounding are the two most commonly used modification methods for SnO_2. Elemental mixing is mainly used in the field of battery research, and different types of elements can achieve different modification effects: Sb[18] and Yb[19] can improve the conductivity, Ag[20] can improve the arc erosion performance, and Er[21] and Pb[22] can improve the optical emission performance. A semiconductor composite is commonly used in the field of photocatalysis, such as TiO_2,[23] $Bi_{12}O_{15}Cl_6$,[24] $g\text{-}C_3N_4$ (ref. 25) and other heterojunctions formed with SnO_2 which reduce the photogenerated hole–electron recombination rate, and broaden the photocatalytic performance in the visible light range. Metal sulfides are important narrow-band-gap semiconductor materials which typically have excellent visible light absorption ability.[26] One of them, silver bromide (AgBr), is a good candidate for SnO_2 photosensitization due to its fast charge exchange properties, narrow band gap and high stability as a non-toxic semiconductor.

This study uses a hydrothermal procedure and an *in situ* precipitation method to prepare an SnO_2–AgBr composite photocatalyst that responds to visible light. It is known that the composite molar ratio between SnO_2 and AgBr is one of the main factors affecting its optical catalytic activity, so using methyl orange (MO) and malachite green (MG) as target

---

[a] *College of Civil Engineering, Guizhou University, Guiyang, 555000, PR China. E-mail: dhengcan@163.com*

[b] *POWERCHINA Guizhou Electric Power Engineering Co., Ltd, Guiyang, 555000, PR China*

[c] *Guizhou Polytechnic of Construction, Guiyang, 551400, PR China*

pollutants, the effect of a high molar ratio on photocatalytic activity was investigated. Through the influence of composite dosage, pH and humic acid concentration on degradation efficiency, the stability of the photocatalyst to a water environment was demonstrated, and a Z-scheme mechanism of the SnO_2–AgBr composite was proposed, and the degradation pathways of MO and MG were speculated upon.

2. Experiment

2.1 Preparation of SnO_2

All chemicals were of analytical purity and used without further purification. A certain amount of $SnCl_4 \cdot 5H_2O$ was dissolved in 40 mL of deionized water and magnetically stirred for 60 min. NaOH was added to adjust the pH to 10 and then stirring continued for 30 min. The final product was obtained by hydrothermal reaction at 180 °C for 10 h. The SnO_2 crystals were washed alternately with deionized water and anhydrous ethanol 3 times, and baked at 90 °C until dry.

2.2 Preparation of SnO_2–AgBr

0.46 g of SnO_2 was dissolved in 40 mL of deionized water; then 30 mL of 0.1 mol L^{-1} $AgNO_3$ solution was added, and stirred for 30 min. 0.36 g of KBr was dissolved in 40 mL of deionized water, and then the KBr solution was slowly added to the above mixture and stirred away from light for 3 h. After the sediment was filtered and washed with deionized water and heated at 130 °C for 20 h, an SnO_2–AgBr composite with a molar ratio of 1 : 1 could be obtained, which is denoted SnO_2–AgBr (1 : 1). The above steps were repeated to prepare composites with molar ratios of SnO_2 and AgBr of 1 : 2 and 2 : 1, denoted SnO_2–AgBr (1 : 2) and SnO_2–AgBr (2 : 1), respectively.

2.3 Characterization and instrumental parameters

In this experiment, the crystallinity of the sample was characterized with a D8 ADVANCE X-ray diffractometer (XRD), Kα radiation ($\lambda = 1.5406$ A) Cu target; the diffraction angle ranged from 10° to 80°. An SU8220 cold field emission scanning electron microscope (SEM) was used to characterize the structure and composition of the samples. The sample crystal was analyzed with a Talos F200S transmission electron microscope (TEM), and the chemical bond of the sample was analyzed by ESCALAB 250 X-ray photoelectron spectroscopy (XPS), where the binding energy in the spectrum was calibrated by C1s (284.62 eV). A 1290II-6460 liquid mass coupling instrument (HPLC-MS) was used to analyze the composition of the samples, in which the current was 10 μA and the voltage was 15 kV. An F-7100 Spectrometer (PL) tested the photoluminescence spectra. The light absorption properties of the materials were analyzed with a UV-3600 type UV-visible spectrophotometer. The electrochemical impedance spectroscopy (EIS) was measured at V_{oc} one-sun illumination with 0.1 M Na_2SO_4 electrolyte between a Pt-coated film counter electrode and sample film coated on fluorine-doped tin oxide (FTO) as a working electrode, held by two heavy-duty clips.

2.4 Photocatalytic experiments

A 500 W tungsten halogen lamp ($\lambda > 420$ nm) was used as the visible light source, and 100 mL (30 mg L^{-1}) of the MO/MG solution were added into the reactor. The temperature of the reaction solutions was kept constant by the actions of a magnetic blender and a cooling system. The SnO_2–AgBr composites were weighed (0.1 g) and evenly dispersed in the solution. The light source was turned off for the first 30 min so that the catalyst and the target pollutants could achieve adsorption equilibrium. A DR6000 ultraviolet spectrophotometer was used to test the absorbance of MO and MG at 464 nm and 618 nm, respectively, and the concentrations at different times were calculated according to the standard curves of MO and MG, to calculate their degradation rates.

2.5 Cycling experiments

The stability of the catalyst was tested by cycling experiments. The same SnO_2–AgBr (1 : 1) compounds were used to degrade MO/MG for four runs. After the degradation reaction the catalyst was collected, washed alternately with anhydrous ethanol and pure water four times, and then fully dried in a constant temperature drying oven at 90 °C before use.

3. Results and discussion

3.1 Material characterization

3.1.1 XRD analysis. The XRD of SnO_2–AgBr composites with different molar ratios are shown in Fig. 1, in which the crystallinity and purity of the composites can be seen. The main diffraction peaks at 26.58°, 33.88°, 51.75° correspond to the tetragonal SnO_2 (110), (101), (211) crystal faces (PDF#41-1445), and the diffraction peaks at 30.96°, 44.35° correspond to the cubic phase AgBr (200), (220) crystal face (PDF#06-0438).[27,28] There are no other peaks, indicating that SnO_2 and AgBr have high purity. The diffraction peaks position of SnO_2 with different molar ratios did not change, indicating that AgBr did not change the crystal shape of SnO_2 through surface loading. The diffraction peak intensity of AgBr increases with its loading capacity, but excessive AgBr led to an increase in the photogenerated hole–electron pair recombination rate and a decrease in photocatalytic degradation activity.[29] The XRD results showed that SnO_2 and AgBr were successfully prepared.

3.1.2 SEM and TEM analysis. The morphology and structure of the sample can be observed through SEM (Fig. 2a and b), showing that SnO_2 consists mainly of a porous structure composed of irregular ellipsoids with different particle sizes, and the uneven gully structure on the surface provides support for the load of AgBr. As can be seen from Fig. 2c–e, there is local agglomeration of SnO_2–AgBr (1 : 2) due to excessive AgBr, but no significant agglomeration of SnO_2–AgBr (1 : 1) or SnO_2–AgBr (2 : 1) can be observed due to the small size, small load and high dispersion of AgBr.

SnO_2–AgBr (1 : 1) TEM (Fig. 2f–i) proved that SnO_2 and AgBr were successfully combined, but there was a small amount of agglomeration in AgBr (Fig. 3f and g), which was an objective result of the experimental conditions. The lattice spacings of

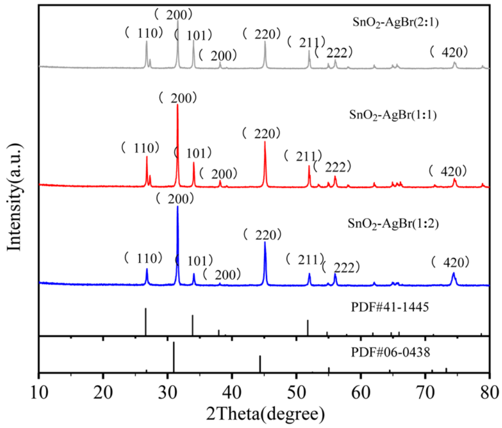

Fig. 1 XRD of SnO_2–AgBr composites with different mole ratios.

0.26 nm and 0.33 nm correspond to the (101) and (110) crystal faces of SnO_2, respectively (Fig. 2h); the lattice spacings of 0.26 nm and 0.20 nm correspond to the crystal faces of SnO_2 (101) and AgBr (220), respectively (Fig. 2i).[30–32]

3.1.3 EDS analysis. In order to understand the chemical composition and elemental distribution of the composite, EDS of SnO_2–AgBr (1 : 1) was performed (Fig. 3). The results showed that the composite was composed of Sn, O, Ag and Br, and no other elements were detected. AgBr particles are evenly distributed on the surface of SnO_2, and there is no large-scale agglomeration. The theoretical percentage of Ag and Br atoms is relatively low, which may be caused by the existence of a small amount of AgBr agglomeration during the preparation process.

3.1.4 XPS analysis. In order to investigate the elemental composition and valence state of the SnO_2–AgBr composite, as well as the binding state of AgBr and SnO_2 crystals, XPS of SnO_2 and SnO_2–AgBr (1 : 1) was performed; all spectra were based on C1s (284.4 eV). Fig. 4a shows the full spectra of SnO_2 and SnO_2–AgBr (1 : 1), where one can clearly see the binding energies of Sn 3d, O 1s, Ag 3d and Br 3d. The binding energies at 488.1 eV and 496.5 eV correspond to Sn $3d_{5/2}$ and Sn $3d_{3/2}$, respectively, and the pyrolysis energy difference is 8.4 eV, which proves that Sn is Sn^{4+} in the composite.[33,34] After loading AgBr, the binding energies of Sn 3d are slightly shifted compared with SnO_2,

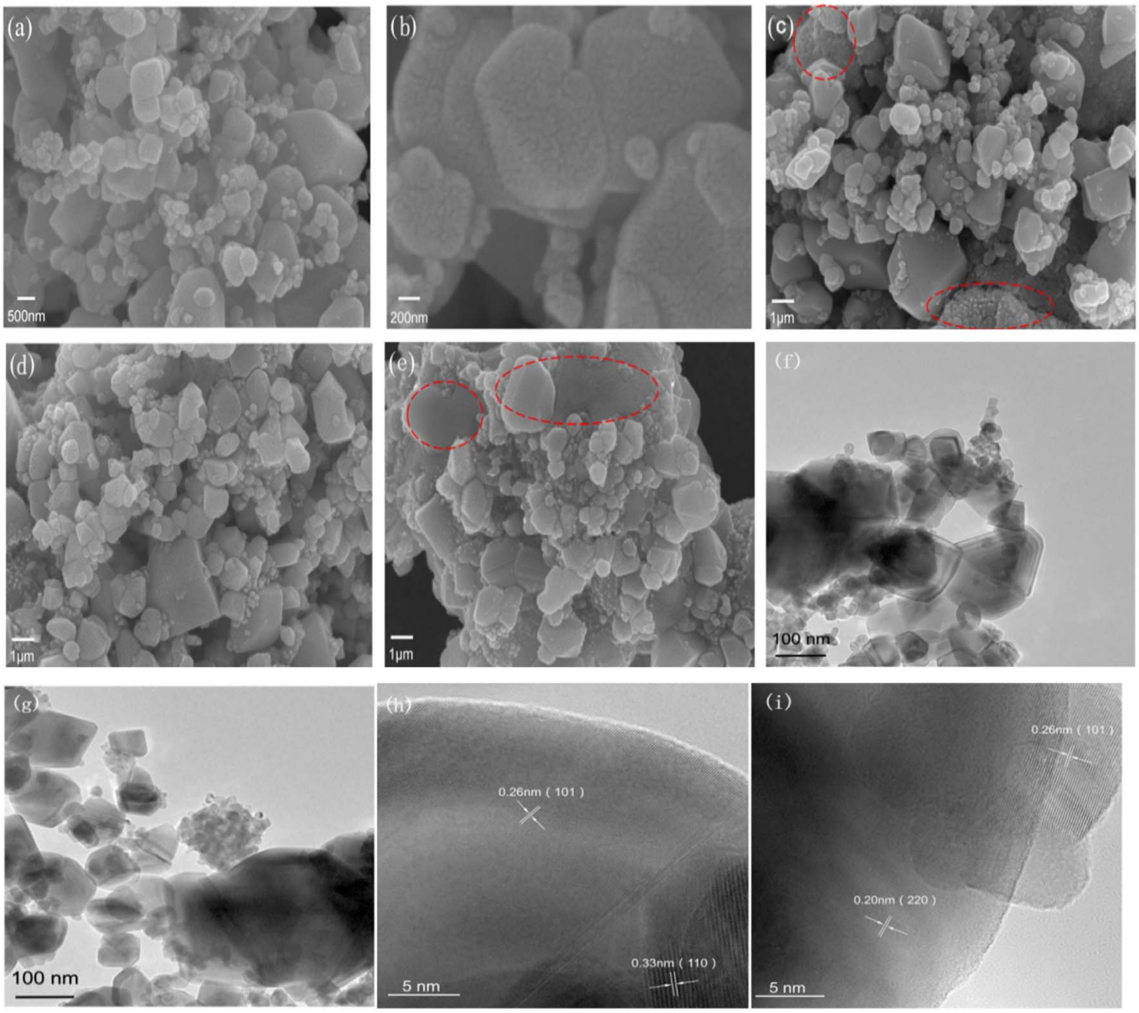

Fig. 2 SEM and TEM of SnO_2 and SnO_2–AgBr: SEM of (a and b) AgBr, (c) SnO_2–AgBr (1 : 2), (d) SnO_2–AgBr (1 : 1), and (e) SnO_2–AgBr (2 : 1); (f–i) TEM of SnO_2–AgBr (1 : 1).

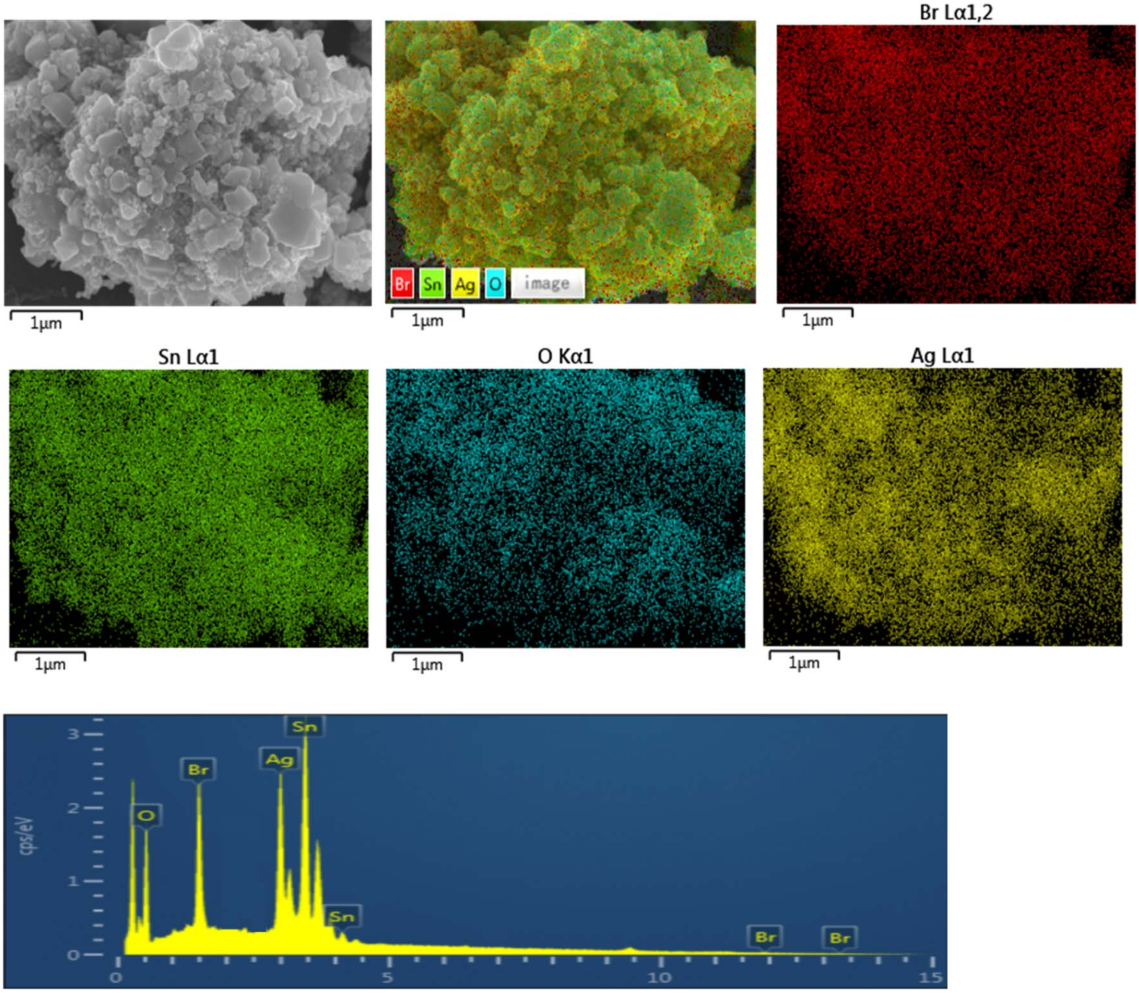

Fig. 3 EDS of the SnO_2–AgBr (1 : 1) composite.

which may be because the electron cloud density of Sn is changed when AgBr and SnO_2 combine with each other, which affects the electronic structure of SnO_2.[35] The binding energy of O1s at 529.6 eV corresponds to the lattice oxygen of Sn–O, and that at 530.9 eV corresponds to water species adsorbed on the surface of the as-prepared sample. These two reactive oxygen species will promote the formation of ·OH and $\cdot O_2^-$ and facilitate the oxidative decomposition of organic matter.[36,37] After loading AgBr, the binding energies of O 1s are shifted in the high-energy direction relative to SnO_2, indicating that the composite has more oxygen vacancies, which can improve the separation of electron–hole pairs and increase the photocatalytic efficiency.[38] Binding energies at 367.8 eV and 373.9 eV correspond to $Ag3d_{5/2}$ and $Ag3d_{3/2}$, respectively.[39,40] In a summary of previous reports,[41,42] binding energies at 367.3 eV and 374.2 eV are attributed to Ag^0; those at 367.8 eV and 373.8 eV are attributed to Ag^+. Therefore, the valence state of Ag in the composite is Ag^+. The binding energies at 67.8 eV and 68.8 eV correspond to Br $3d_{5/2}$ and Br $3d_{3/2}$, respectively, indicating that the valence state of Br in the composite is Br^-.[43] In summary, SnO_2 and AgBr were successfully bonded by chemical bonds.

3.1.5 UV-vis and PL analysis. The degree of response of the composite to light and the recombination efficiency of photogenerated electron–hole pairs are two main factors with which to measure the efficiency of photocatalytic materials. The light absorption range of the composite is reflected by UV-vis, and the photogenerated hole–electron recombination rate by PL emission spectroscopy. The absorption edge of SnO_2 is around 340 nm, and it hardly responds to visible light. The absorption curve of AgBr does not decrease significantly in the range of 200–800 nm, and it still maintains a high absorption intensity (Fig. 5a). Compared with SnO_2–AgBr with different molar ratios, the absorption curve of SnO_2 is obviously redshifted towards the visible region, indicating that the load of AgBr effectively improves the ability of SnO_2 to respond to visible light.[44] The absorption intensity of the composite for visible light increased first and then decreased with AgBr load, and SnO_2–AgBr (1 : 1) showed the best light absorption intensity and range. The results indicate that visible light can be used more effectively and more photogenerated electron–hole pairs can be generated, which are beneficial to the enhancement of photocatalytic activity.[45,46] The band-gap width is calculated (Fig. 5b according to the Kubelka–Munk function). The band-gap widths of SnO_2,

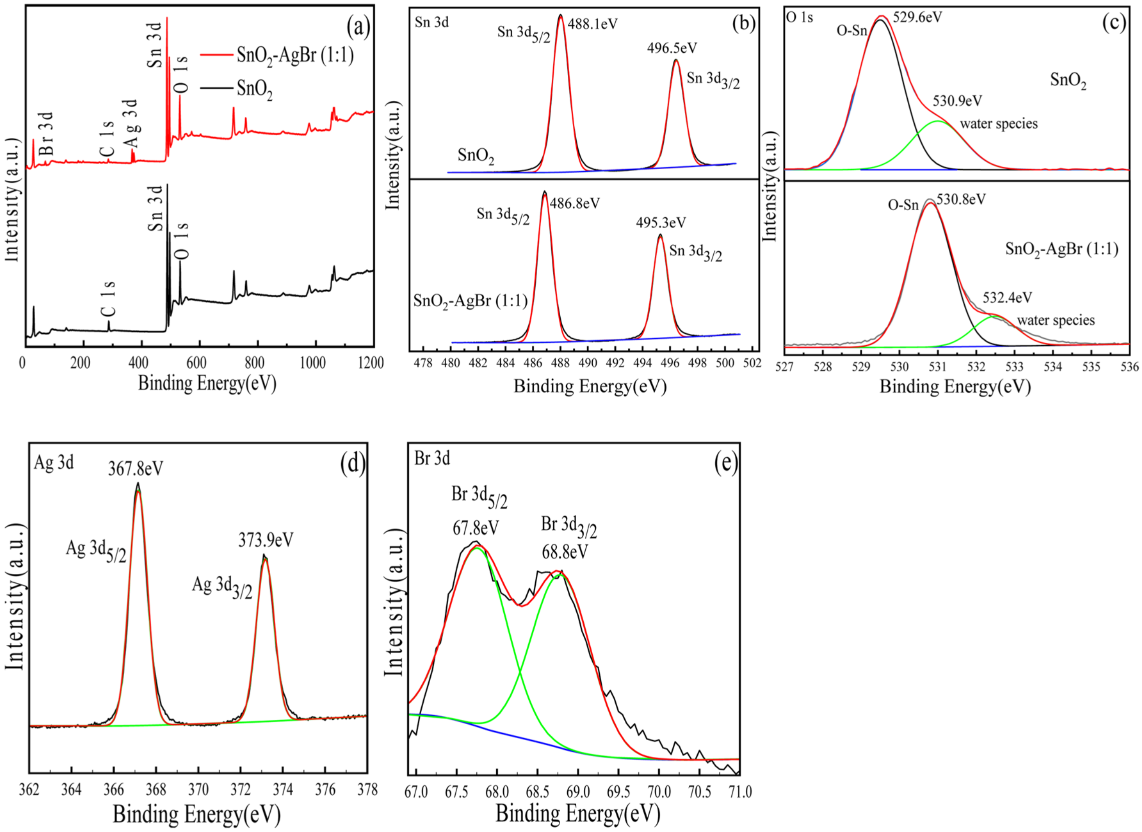

Fig. 4 XPS of SnO_2 and SnO_2–AgBr (1 : 1): (a) full survey spectra, (b) Sn 3d, (c) O 1s, (d) Ag 3d, and (e) Br 3d.

AgBr, SnO_2–AgBr (1 : 2), SnO_2–AgBr (1 : 1) and SnO_2–AgBr (2 : 1) are 3.51 eV, 2.6 eV, 2.75 eV, 2.62 eV and 2.80 eV, respectively.

PL results show that SnO_2–AgBr with different molar ratios have diffraction peaks at 460 nm (Fig. 5c), but the SnO_2–AgBr (1 : 1) composite has the lowest diffraction peak intensity, indicating the lowest electron–hole recombination efficiency and the longest photogenerated carrier lifetime.[47,48] In summary, SnO_2–AgBr (1 : 1) has the best photocatalytic performance compared with other molar ratio composites.

3.1.6 Zeta potential test. In order to investigate the charging property of the composite surface and its dispersion in water, a particle size analyzer was used to detect the zeta potential of the SnO_2–AgBr composite, and the results are shown in Fig. 6a. The zero points of SnO_2–AgBr (1 : 2), SnO_2–AgBr (1 : 1) and SnO_2–AgBr (2 : 1) are 4.61, 5.22 and 6.18, respectively. Under neutral conditions, the surface of SnO_2–AgBr is electronegative, which is theoretically more conducive to attracting cationic MB, and has an electrostatic repulsive effect on anionic MO.[49,50]

Electrochemical impedance spectroscopy (EIS) analysis was carried out to determine the electron transport properties of SnO_2–AgBr that eventually influenced the performance of SnO_2–AgBr. It can be seen from Fig. 6b that the impedance radius of SnO_2 is the largest and that of SnO_2–AgBr (1 : 1) is the smallest, indicating that SnO_2–AgBr (1 : 1) has the smallest charge

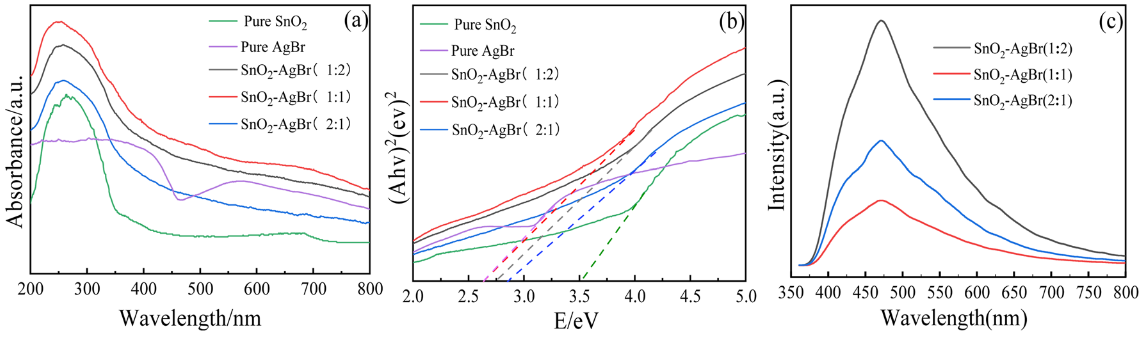

Fig. 5 (a) UV-vis and (b) band-gap width of SnO_2 and SnO_2–AgBr composite; (c) PL of SnO_2–AgBr composite.

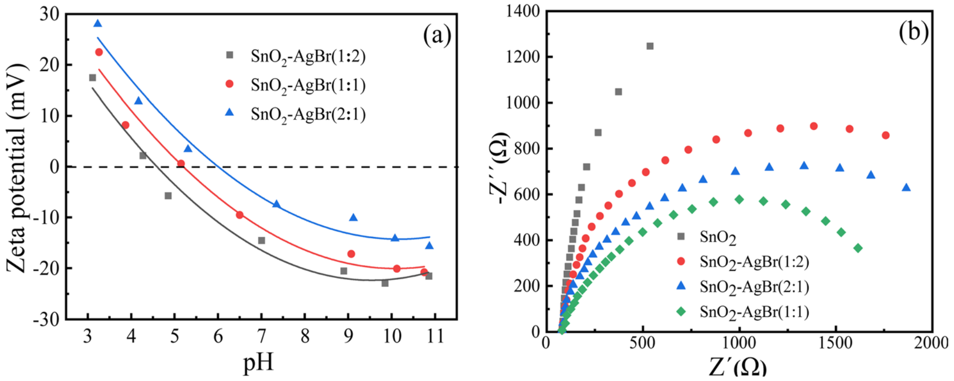

Fig. 6 Zeta potential (a) and electrochemical impedance curve (b) of the SnO_2–AgBr composite.

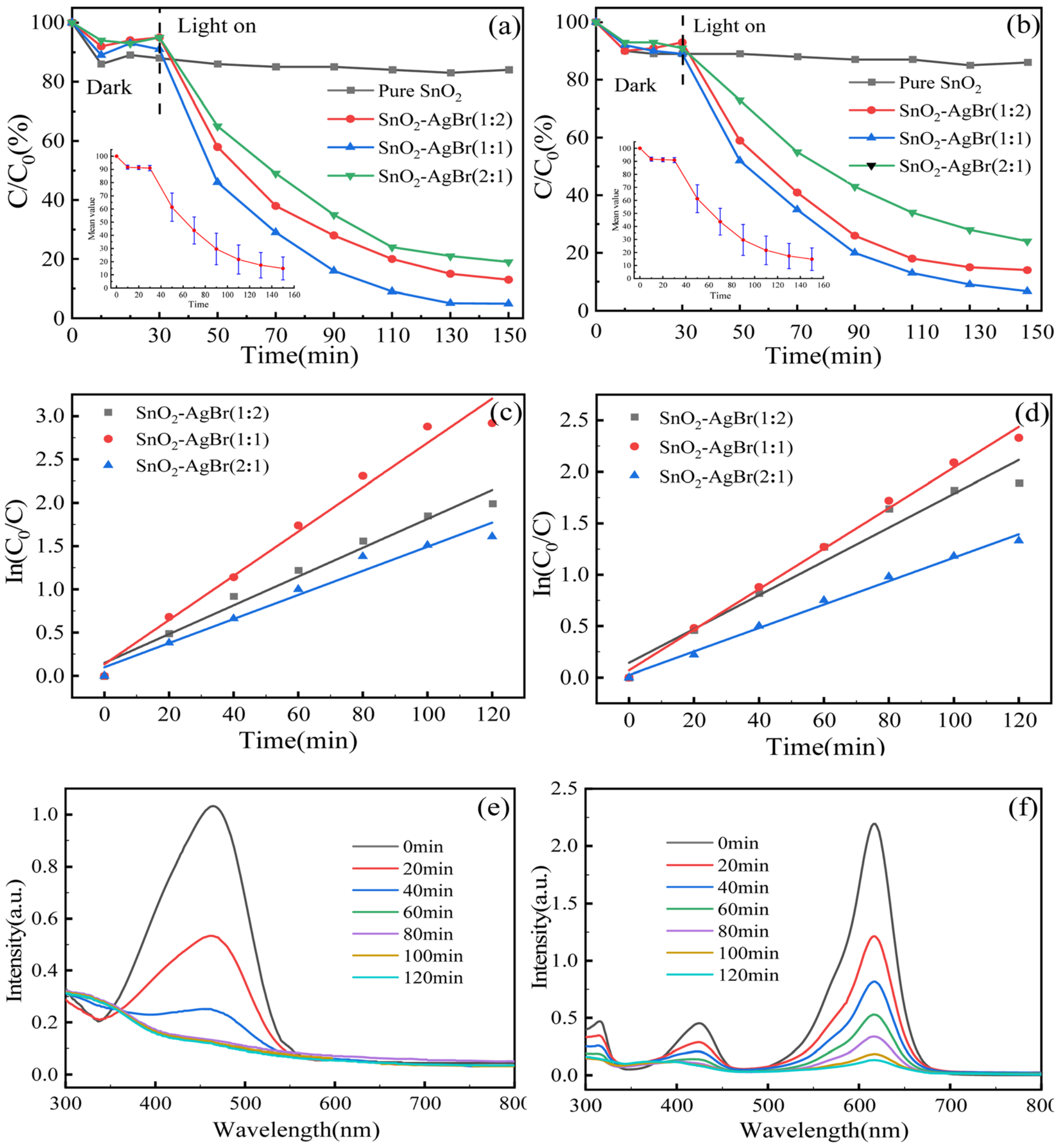

Fig. 7 Photocatalytic degradation by the composite with different molar ratios for (a) MO and (b) MG; first-order kinetics of (c) MO and (d) MG; UV-vis absorption spectra of (e) MO and (f) MG.

transfer resistance and the highest separation efficiency, which is consistent with the PL result.

3.2 Photocatalytic degradation experiment

3.2.1 Degradation analysis of target pollutants. As shown in Fig. 7a and b, the dark adsorption of the composite with different molar ratios for MO and MG is about 10%, which contradicts the conclusion of the zeta potential analysis. Therefore, it is speculated that electrostatic effect does not play a major role in the adsorption process. In the photoreaction phase, SnO_2 had little degradation effect on MO or MG, which was consistent with the UV-vis analysis. The photocatalytic degradation rate of SnO_2–AgBr was significantly increased because of the formed heterojunction. SnO_2, as a photogenerated electron acceptor, could inhibit the photogenerated electron–hole recombination rate and improve the contact between active substances and pollutants.[51,52] SnO_2–AgBr (1 : 1) had the best degradation effect on MO and MG, and the 150 min treatment rates were 96.74% and 93.36%, respectively. A dynamic analysis of degradation rate (Fig. 7c and d) showed that the k of MO and MG were $2.56 \times 10^{-2}\ \text{min}^{-1}$ and $2.01 \times 10^{-2}\ \text{min}^{-1}$, respectively, which were 1.83 and 1.77 times those of SnO_2–AgBr (2 : 1), 1.53 and 1.22 times those of SnO_2–AgBr (1 : 2). The results indicated that SnO_2–AgBr (1 : 1) had the fastest degradation rate for the two pollutants.[53] The photocatalytic degradation rate of SnO_2–AgBr (1 : 2) decreased because the active site on the surface of the composite was shielded due to excessive AgBr attachment to the surface of SnO_2. At the same time, the light penetration was weakened and the absorption of visible light was affected by the composite.[54–56] UV-vis absorption spectra of MO and MG (Fig. 7e and f) reflect the photocatalytic degradation process. The intensity of the absorption peaks at 464 nm and 618 nm gradually decreased and eventually disappeared with reaction time, indicating that the pollutants were degraded.

3.2.2 The influence of composite dosage. In the treatment of wastewater, the catalyst is often one of the main costs in the advanced stage of water treatment. Under the condition of pH = 7, 100 mL MO and MG solution with a concentration of 30 mg L^{-1} were added with 0.05 g, 0.08 g, 0.10 g, 0.12 g and 0.15 g SnO_2–AgBr (1 : 1) composite. The relationship between the dosage of the composite and the treatment efficiency was investigated within 150 min. As shown in Fig. 8, when the dosage increased from 0.5 g L^{-1} to 1.5 g L^{-1}, the degradation rates of MO and MG increased from 54.42% and 59.85% to 97.76% and 96.32%, and the k increased by 4.58 and 3.65 times, respectively. In this experiment, there was no phenomenon where photocatalytic activity decreased due to excessive composite addition, which affected the transparency of the solution.[57,58]

3.2.3 Influence of humic acid concentration. Humic acid (HA) is produced by the decomposition of natural organic compounds and exists in all sewage, so it has a great influence on the form of existence and migration performance for some pollutants in water.[59,60] In order to investigate the effect of HA concentration on catalyst degradation efficiency, HA concentrations were set at 0 mg L^{-1} (blank control), 5 mg L^{-1}, 10 mg L^{-1} and 20 mg L^{-1}. The experimental results are shown

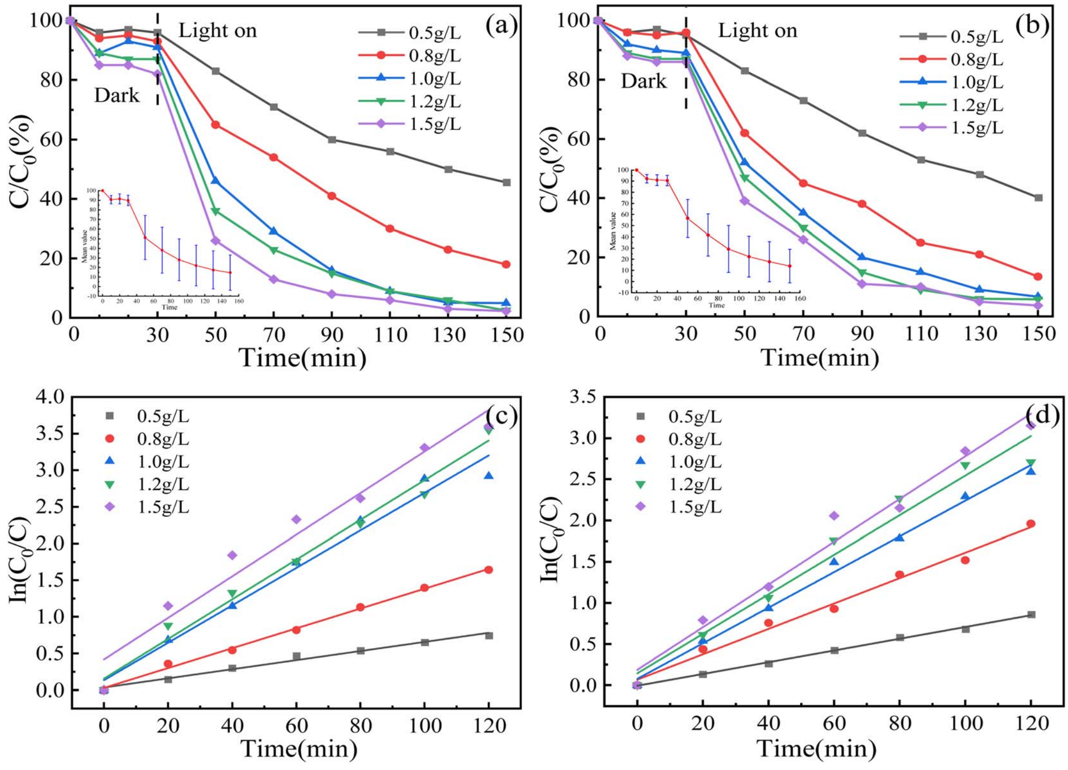

Fig. 8 Effect of composite dosage on degradation rate of (a) MO and (b) MG; first-order kinetics of (c) MO and (d) MG.

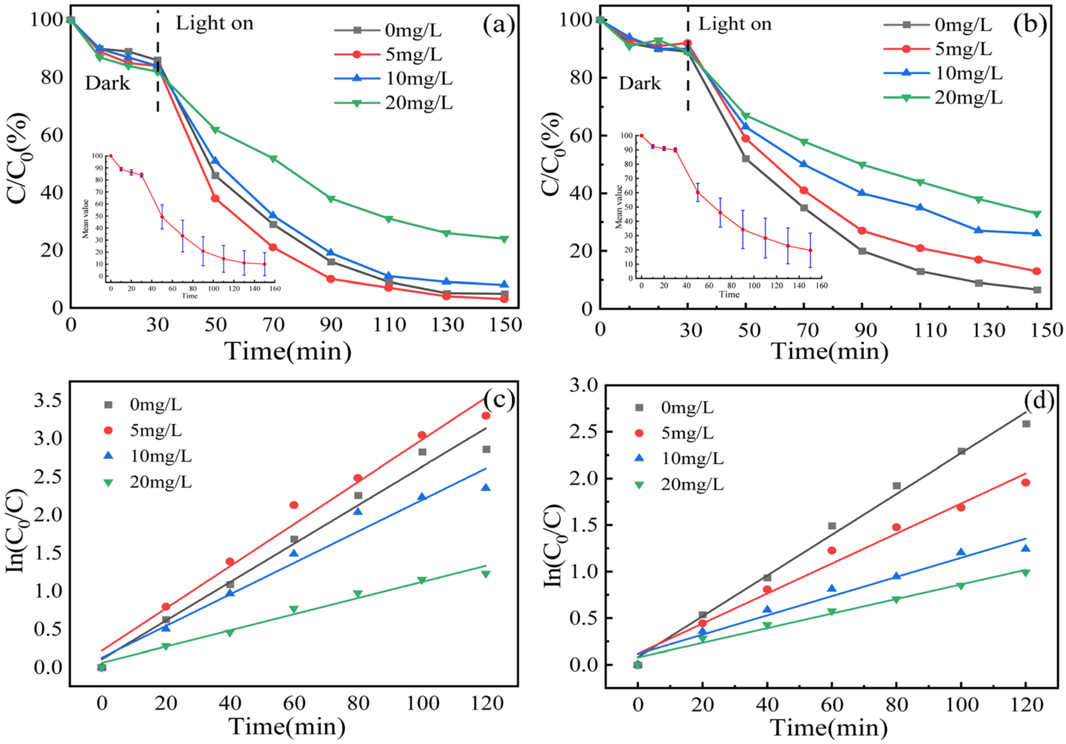

Fig. 9 Effect of humic acid on degradation rate for (a) MO and (b) MG; first-order kinetics of (c) MO and (d) MG.

in Fig. 9. When the concentration of HA increased from 0 mg L^{-1} to 5 mg L^{-1}, it promoted the degradation rate of MO, and inhibited it as the concentration continued to increase. However, it has consistently shown inhibitory effects on MG. The reason is that HA can be used as a photosensitizer to promote the production of active substances, thereby

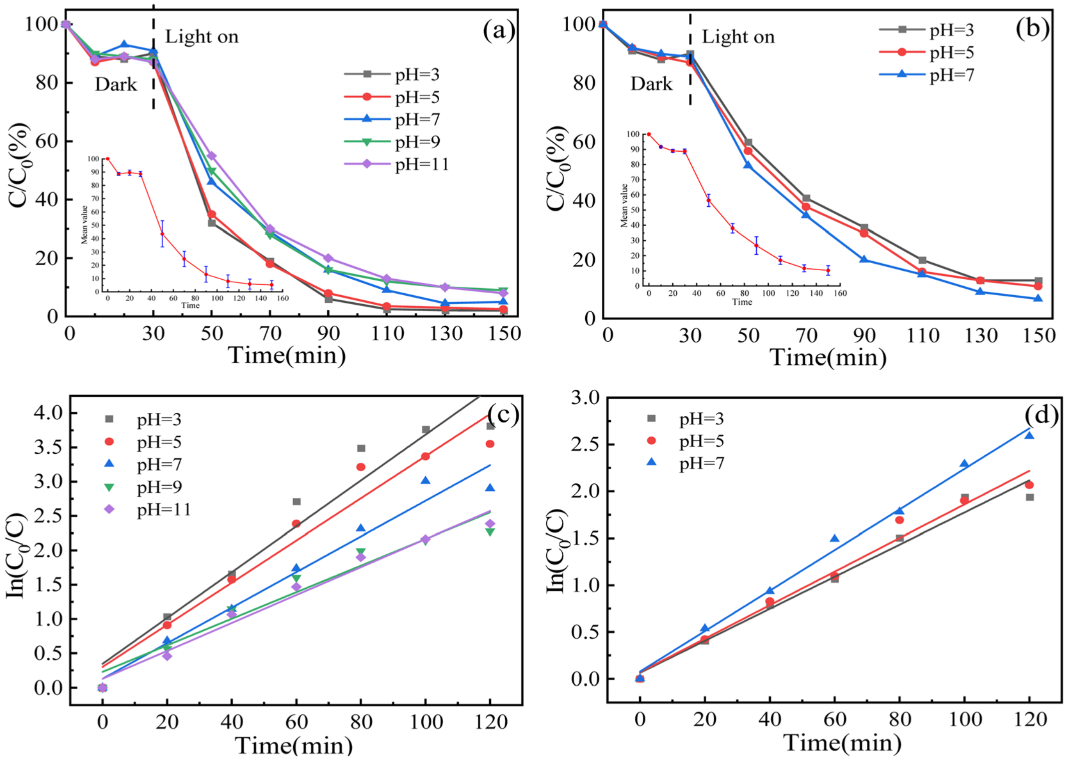

Fig. 10 Effect of pH on degradation rate for (a) MO and (b) MG; first-order kinetics of (c) MO and (d) MG.

improving the degradation rate of MO and MG. However, it also forms a competitive relationship with MO and MG for active substances, or becomes a quenching agent, reducing the content of active substances.[61–63] In this experiment, the two target pollutants show different experimental results, which is the competitive effect of HA.

3.2.4 Influence of pH.

pH is a very important parameter in water treatment, which can affect the efficiency of water treatment by changing the surface adsorption capacity of a catalyst or the hydrolyzed form of pollutants.[64,65] The relationship between pH and degradation efficiency was investigated when the pH was 3, 5, 7, 9 and 11, and the dosage of the composite was 0.1 g. The results are shown in Fig. 10: with an increase in pH, the photocatalytic degradation rate of MO and MG has little effect, but the k of MO decreases continuously. The reason is that under neutral and alkaline conditions, MO is an azo structure containing N═N double bonds with a bond energy of 456 kJ mol^{-1}, while under acidic conditions, the N═N double bonds are transformed into N–N single bond quinone structures with a bond energy of 159 kJ mol^{-1}. Therefore, the reduction in bond energy under acidic conditions leads more easily to the decomposition of MO.[66,67]

It was found that under alkaline conditions, MG was converted to colorless tertiary alcohol, resulting in the solution rapidly fading from blue-green to colorless.[68,69] Due to the limitations of the experimental conditions, absorbance cannot be tested, so only acid and neutral conditions were investigated. The degradation effect of MG under acidic conditions is slightly decreased compared with that under neutral conditions, because H$^+$ consumes the active substance ·OH or occupies the active site under acidic conditions.[70] At the same time, with a change in pH, the adsorption properties of the composite for MG and MO showed almost no change, which proved that the adsorption process was not dominated by electrostatic action, but by the hydraulic action of surface complexation or magnetic agitation.

3.3 Repeated experiments

The stability of the SnO$_2$–AgBr (1 : 1) composite is related to its practicability and is also an important factor to measure its photocatalytic performance.[71,72] After four cycles of experiment, the degradation rates of MO and MG decreased to 66.42% and 70.86%, respectively (Fig. 11a and b). The samples collected after four cycles were tested by XRD, and the characterization results are shown in Fig. 11c and d. The position and intensity of the diffraction peak of SnO$_2$–AgBr (1 : 1) did not change significantly, but the new diffraction peak at 38.25° corresponds to Ag^0.[73] AgBr is corroded by light and some Ag$^+$ is restored to Ag^0, which covers part of the active site. This is the main reason for the continuous decline in photocatalytic activity with repeated experiments.[74,75]

3.4 Free radical trapping experiment

The main active substances were determined by a free radical trapping experiment, and the degradation mechanism of SnO$_2$–AgBr (1 : 1) was further studied. Isopropyl alcohol (IPA), *p*-benzoquinone (BQ) and ammonium oxalate (AO) were used as inhibitors of ·OH, ·O$_2^-$ and h$^+$, respectively.[76,77] The dosage of BQ was 1 mmol L^{-1}; those of IPA and AO were 10 mmol L^{-1}. The

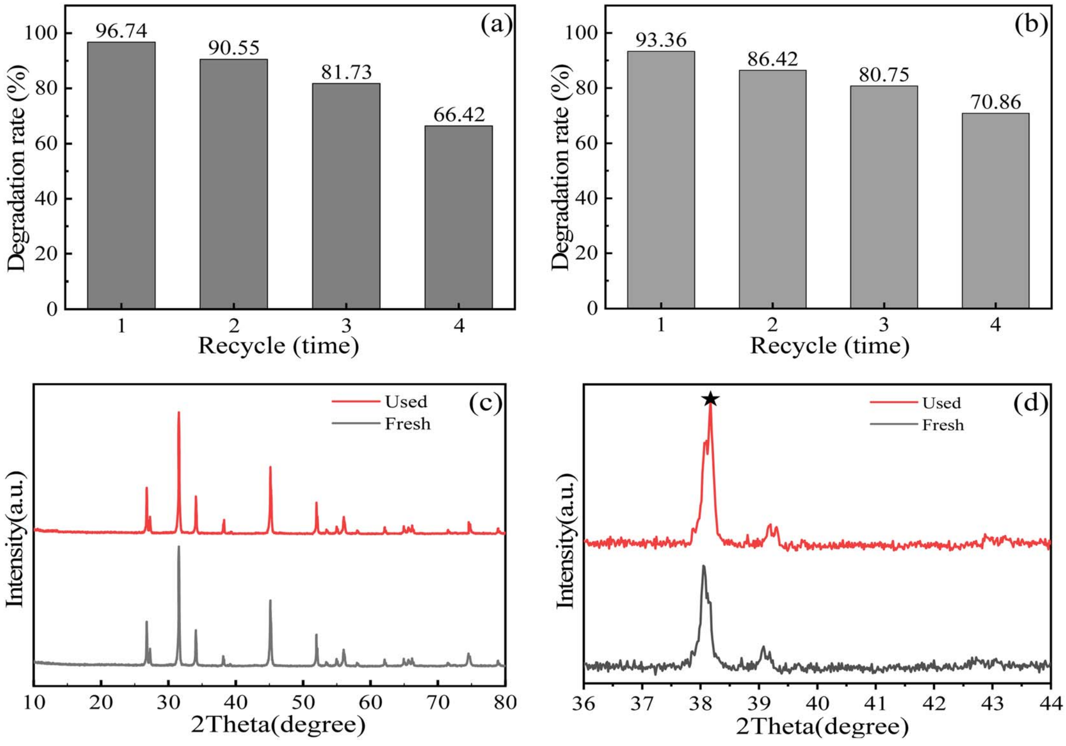

Fig. 11 Composite repeated experiments for (a) MO and (b) MG; (c and d) XRD of composite after repeated experiments.

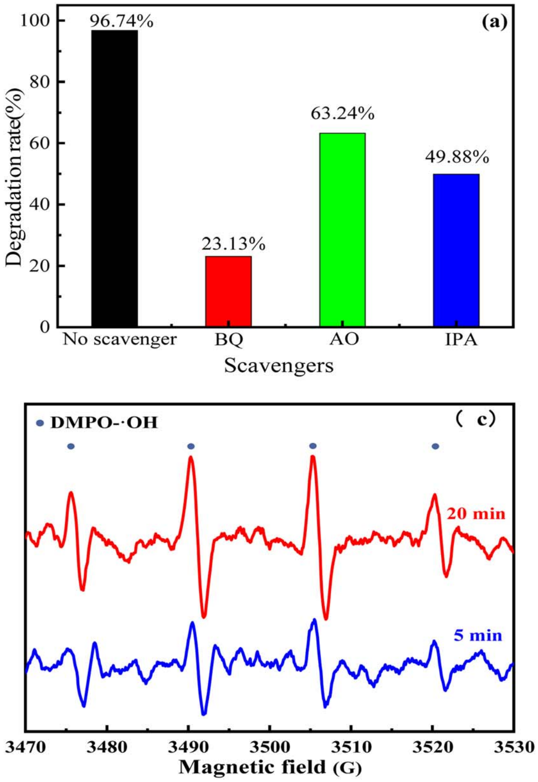

Fig. 12 SnO_2–AgBr (1 : 1) composite trapping experiments for (a) MO and (b) MG; EPR spectra of the SnO_2–AgBr (1 : 1) composite: (c) DMPO–·OH, (d) DMPO–·O_2^-.

results are shown in Fig. 12. The three inhibitors of active species all reduced the degradation efficiency to varying degrees, indicating that ·O_2^-, ·OH and h^+ were involved in photocatalytic degradation. However, after the addition of BQ and IPA, the degradation rate seriously decreased, indicating that ·O_2^- and ·OH were the main active substances, and h^+ played a secondary role. Moreover, these results were further confirmed by electron paramagnetic resonance (EPR) tests with DMPO as the spintrapping reagent. As displayed in Fig. 12c and d, signals of ·OH and ·O_2^- were observed in the SnO_2–AgBr (1 : 1) system and the intensities of the signals gradually became intense with prolonged light illumination time.

3.5 Prediction of degradation mechanism

According to the results of the characterization, the SnO_2–AgBr composite reaction mechanism was deduced from the Mulliken empirical formula (eqn (1) and (2)):

$$E_{VB} = X - E^e + 0.5E_g \tag{1}$$

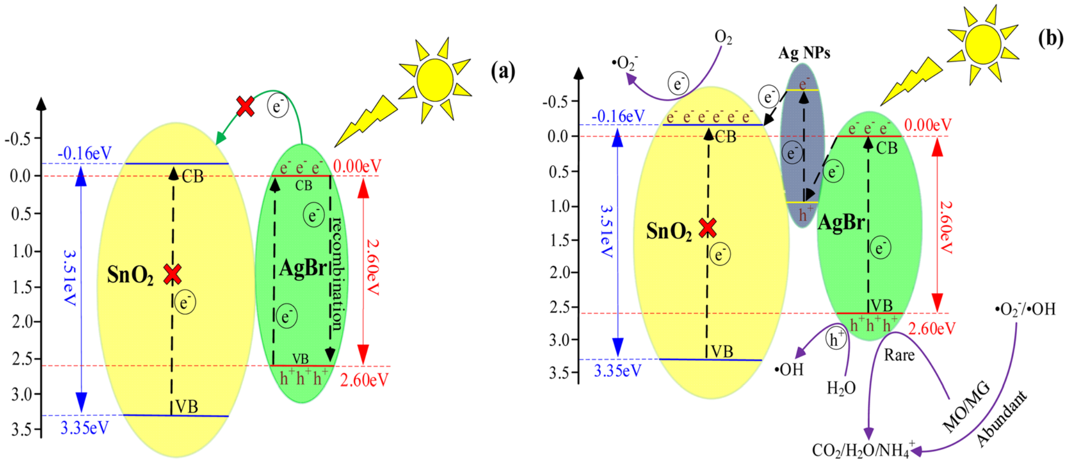

Fig. 13 (a) SnO_2–AgBr (1 : 1) traditional heterojunctions mechanism; (b) Z-scheme mechanism.

$$E_{\mathrm{CB}} = E_{\mathrm{VB}} - E_{\mathrm{g}} \tag{2}$$

where E_{VB} and E_{CB} are the potentials at the top of the valence band and the bottom of the conduction band relative to the standard (H_2) electrode potential, respectively; X is the electronegativity of the semiconductor; E^{e} is the energy of the free electron on the scale of the hydrogen atom (about 4.5 eV); E_{g} is the band-gap width of the semiconductor.

According to UV-vis, the band gaps of SnO_2 and AgBr are 3.51 eV and 2.6 eV, respectively, and the electronegativities are 6.10 eV and 3.90 eV, respectively. The E_{VB} and E_{CB} of SnO_2 are 3.35 eV and −0.16 eV, and those of AgBr are 2.6 eV and 0.0 V.[78,79] SnO_2 has no response to visible light due to its band-gap width of 3.51 eV, and therefore it cannot produce photogenerated electron–hole pairs. Since the E_{CB} (0.00 eV) of AgBr is higher than that of SnO_2 (−0.16 eV), photogenerated electrons cannot migrate from AgBr to SnO_2 (Fig. 13a). Therefore, if the photoinduced electrons and holes migrate by the traditional type-II charge transfer mechanism, the experimental phenomena cannot be explained.

Therefore, a Z-scheme mechanism using Ag as the electronic medium is proposed (Fig. 13b). Under visible light, AgBr is partially reduced to Ag and attached to the surface of the SnO_2–AgBr composite to form Ag@SnO_2–AgBr. Ag has two roles in a Z-scheme mechanism: as an electronic medium and as a photosensitizer.[80,81] From the UV-vis results (Fig. 7a), it can be seen that AgBr responds to visible light, while SnO_2 cannot, so Ag serves as both a photosensitizer and an electronic medium.[82,83] Ag assumed the responsibility for visible light absorption, not SnO_2. The photogenerated electrons (e_{CB1}^-) in the AgBr conduction band combine with the photogenerated holes (h_{VB2}^+) in the highest occupied orbital of Ag, while the photogenerated electrons (e_{CB2}^-) in the lowest unoccupied orbital of Ag migrate to the conduction band of SnO_2. The photogenerated electrons (e_{CB3}^-) are enriched in the conduction band of SnO_2 and the holes (h_{VB1}^+) are enriched in the valence band of AgBr, and the photogenerated hole–electron separation of AgBr is realized (eqn (3)–(10)).

In addition, since the E_{CB} of SnO_2 (−0.16 eV *vs.* NHE) is lower than that of O_2 (−0.046 eV *vs.* NHE), $\cdot O_2^-$ can be produced. Similarly, the E_{VB} of AgBr (2.60 eV *vs.* NHE) is higher than that of OH-/H_2O (2.30 eV *vs.* NHE), and.

·OH can be formed normally. The Z-scheme mechanism of SnO_2–AgBr composite well reveals its superior photocatalytic performance.

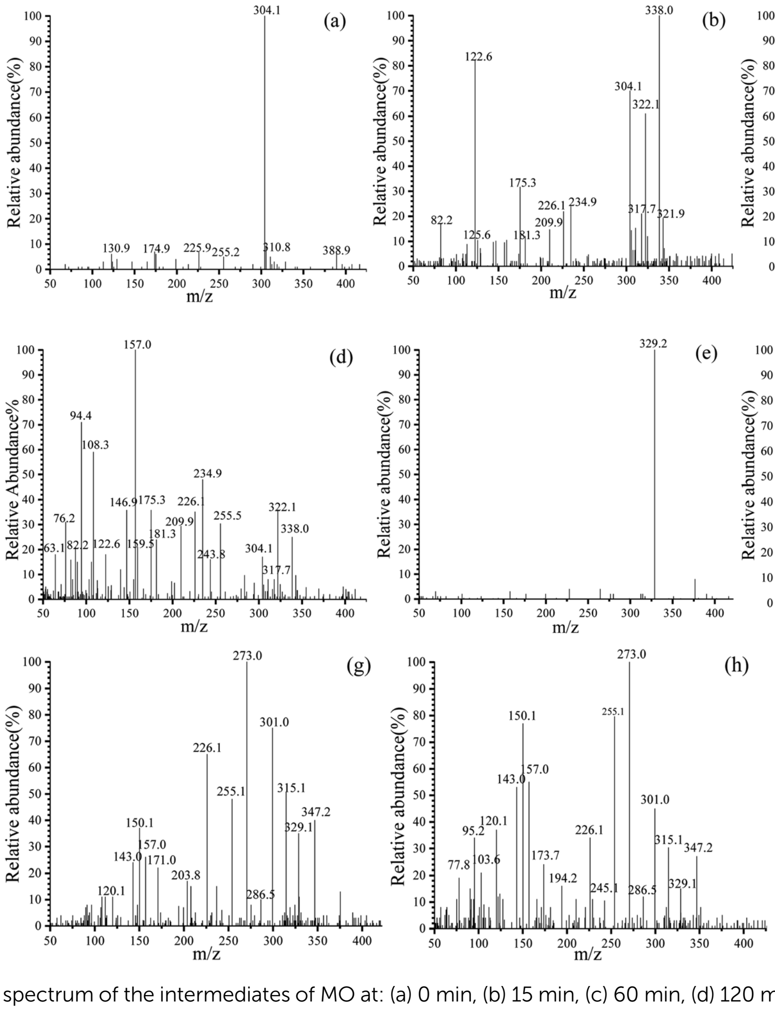

Fig. 14 Mass spectrum of the intermediates of MO at: (a) 0 min, (b) 15 min, (c) 60 min, (d) 120 min; and of MG at: (e) 0 min, (f) 15 min, (g) 60 min, (h) 120 min.

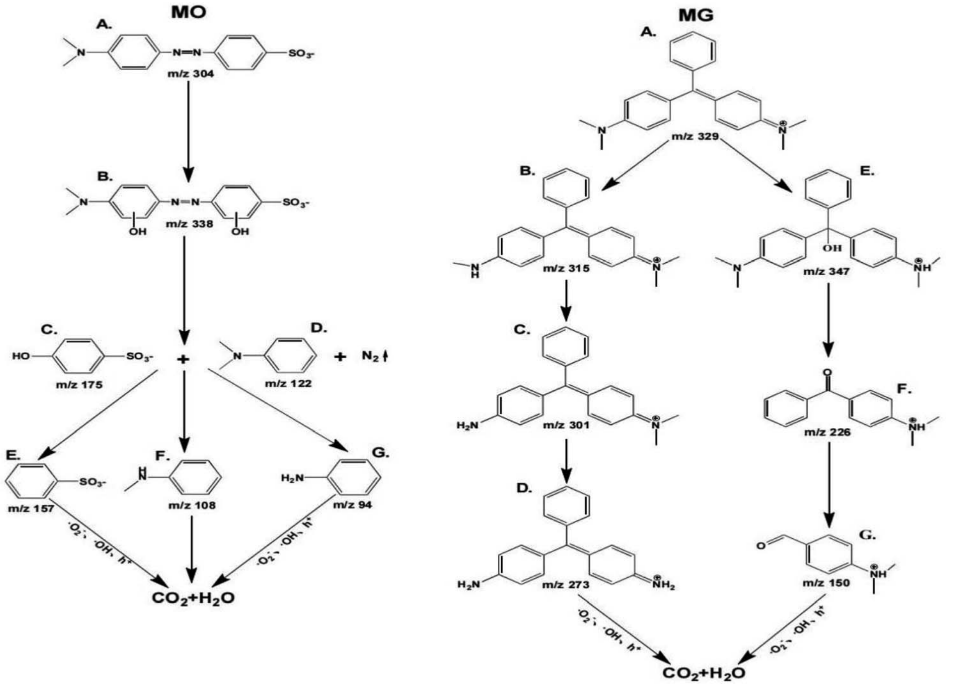

Fig. 15 Prediction of degradation pathways of MO and MG.

$$\mathrm{AgBr} + h\nu \rightarrow e_{CB1}^{-} + h_{VB1}^{+} \tag{3}$$

$$\mathrm{AgBr} + h\nu \rightarrow \mathrm{AgNPs} \tag{4}$$

$$\mathrm{AgNPs} + h\nu \rightarrow e_{CB2}^{-} + h_{VB2}^{+} \tag{5}$$

$$e_{CB1}^{-} + h_{VB2}^{+} \rightarrow \text{recombination} \tag{6}$$

$$e_{CB2}^{-} + \mathrm{AgNPs} \rightarrow \mathrm{SnO_2} + e_{CB3}^{-} \tag{7}$$

$$h_{VB1}^{+} + \mathrm{H_2O} \rightarrow \cdot\mathrm{OH} + \mathrm{H^+} \tag{8}$$

$$e_{CB3}^{-} + \mathrm{O_2} \rightarrow \cdot\mathrm{O_2}^{-} \tag{9}$$

$$\cdot\mathrm{OH}/\cdot\mathrm{O_2}^{-}/\mathrm{h}^{+} + \mathrm{MO/MG} \rightarrow \text{intermediate product} + \mathrm{CO_2} + \mathrm{H_2O} \tag{10}$$

3.6 Prediction of photocatalytic degradation pathway

In order to further study the degradation process of MO/MG, samples of 0 min, 15 min, 60 min and 120 min were taken for HPLC-MS analysis, and the results are shown in Fig. 14. At $t = 0$, *m*/*z* 304.1 is the diffraction peak of MO (Fig. 14a), which is an ionic state formed when MO molecules dissolve in water and remove $\mathrm{Na^+}$, while *m*/*z* 329.2 corresponds to the characteristic peak of MG (Fig. 14e).[84,85] With the progress of the reaction, it was found that the diffraction peaks of MO and MG were significantly reduced and gradually transformed into small molecules. The main *m*/*z* of MO were 338.0, 175.3, 122.6, 157.0, 108.3 and 94.4, while the *m*/*z* of MG were 347.2, 329.2, 315.1, 301.0, 273.0, 226.1 and 150.1.

Based on the *m*/*z* generated in different times, the degradation pathways for MO were proposed (Fig. 15 MO). The benzene ring in **A** (*m*/*z* 304.1) is substituted by ·OH to form product **B**;[86] **B** is attacked by active substances; the C–N bond breaks due to low bond energy, forming products **C**, **D** and $\mathrm{N_2}$;[87] **C** removes ·OH to form product **E**; and **D** generates products **F** and **G** by demethylation.

The degradation pathways of MG (Fig. 15 MG) are: first, **A** (*m*/*z* 329) generates **B** through demethylation, which is the main pathway of photocatalytic degradation and mineralization.[88] Subsequently, **B** is further demethylated to produce **C** and **D**; second, **A** (*m*/*z* 329) undergoes decarboxylation to form **E**; the covalent bond between the benzene ring and the central carbon atom is broken, forming **F**; **G** is formed by debenzenization of **F**. Subsequently, the intermediate of MO/MG will be degraded into $\mathrm{CO_2}$ and $\mathrm{H_2O}$.

4. Conclusions

An $\mathrm{SnO_2}$–AgBr composite showing a Z-scheme mechanism was successfully prepared by a simple hydrothermal procedure and *in situ* precipitation method. Characterization and photocatalytic experiments showed that the composite performance was best when the molar ratio of $\mathrm{SnO_2}$ to AgBr was 1 : 1. The Z-scheme mechanism reduces the photogenic hole–electron recombination rate of AgBr, and produces a large number of ·OH, $\cdot\mathrm{O_2}^{-}$ and $\mathrm{h^+}$, and the degradation rates of simulated MO and MG wastewater reach 96.74% and 93.36%, respectively. Different factors have different effects on the degradation efficiency of simulated dye wastewater. The effect of pH on the degradation rate was small, indicating that the composite had good acid–alkali resistance. The degradation rate increased with composite dosage, and the humic acid concentration was negatively correlated with the degradation rate, which played an inhibitory role. According to mass spectrometry analysis, the degradation pathway of MO and MG proceeded through bond-breaking oxidation, ring-opening and deep oxidation decomposition into intermediate products, and finally degradation into CO_2 and H_2O. The repeatability results of SnO_2–AgBr are not very good, because the silver-based photocatalyst easily undergoes photocorrosion. It is hoped that this study can provide a reference scheme for the design and preparation of a new Z-scheme mechanism, and realize the more efficient, economical and green application of photocatalysis in the field of water treatment.

Conflicts of interest

There are no conflicts to declare.

Acknowledgements

The authors acknowledge the support of Xiaoliang Yang, Yukai Wang and Fei Tang, and their friends in College of Civil Engineering, Guizhou University, Guiyang, China.

References

1 A. Shahi, B. N. Rai and R. S. J. A. B. Singh, Biotechnology, Biodegradation of Reactive Orange 16 Dye in Microbial Fuel Cell: An Innovative Way to Minimize Waste Along with Electricity Production, *Appl. Biochem. Biotechnol.*, 2020, **192**(2), 196–210.

2 T. Angelika, M. Kamila and P. Andrzej, Synthetic organic dyes as contaminants of the aquatic environment and their implications for ecosystems: A review, *Sci. Total Environ.*, 2020, **717**(15), 137222.

3 S. Li, C. Wang, Y. Liu, M. Cai, Y. Wang, H. Zhang, Y. Guo, W. Zhao, Z. Wang and X. Chen, Photocatalytic degradation of tetracycline antibiotic by a novel $Bi_2Sn_2O_7/Bi_2MoO_6$ S-scheme heterojunction: Performance, mechanism insight and toxicity assessment, *Chem. Eng. J.*, 2022, **429**, 132519.

4 T. Liu, C. Wang, C. Ding, W. Wang, B. Wang, M. Wang and J. Zhang, The improved photocatalytic antibiotic removal performance achieved on Ir/$WO_{2.72}$ photocatalysts, *Colloids Surf., A*, 2022, **645**, 128891.

5 T. H. A. Nguyen, V. T. Le, V. D. Doan, A. V. Tran, V. C. Nguyen and Y. Vasseghian, Green synthesis of Nb-doped ZnO nanocomposite for photocatalytic degradation of tetracycline antibiotic under visible light, *Mater. Lett.*, 2022, **308**, 131129.

6 Z. H. Diao, S. T. Huang, X. Chen, M. Y. Zou, H. Liu, P. R. Guo, L. J. Kong and W. Chu, Peroxymonosulfate-assisted photocatalytic degradation of antibiotic norfloxacin by a calcium-based Ag_3PO_4 composite in water: Reactivity, products and mechanism, *J. Cleaner Prod.*, 2022, **330**, 129806.

7 X. Hu, Y. Yu, D. Chen, W. Xu, J. Fang, Z. Liu, R. Li, L. Yao, J. Qin and Z. Fang, Anatase/Rutile homojunction quantum dots anchored on g-C_3N_4 nanosheets for antibiotics degradation in seawater matrice *via* coupled adsorption-photocatalysis: Mechanism insight and toxicity evaluation, *Chem. Eng. J.*, 2022, **432**, 134375.

8 Y. Xie, Y. Yu, H. Xie, F. Huang and T. C. J. J. o. h. m. Hughes, 3D-printed heterogeneous Cu_2O monoliths: Reusable supports for Antibiotic Treatmentantibiotic treatment of wastewater, *J. Hazard. Mater.*, 2022, **2**(435), 1–14.

9 X. Zhang, B. Xu, S. Wang, X. Li, B. Liu, Y. Xu, P. Yu and Y. J. J. o. H. M. Sun, High-density dispersion of CuNx sites for H_2O_2 activation toward enhanced Photo-Fenton performance in antibiotic contaminant degradation, *J. Hazard. Mater.*, 2022, **423**, 127039.

10 L. Jing, Y. Xu, J. Liu, M. Zhou and J. Xie, Direct Z-scheme red carbon nitride/rod-like lanthanum vanadate composites with enhanced photodegradation of antibiotic contaminants, *Appl. Catal., B*, 2020, **277**, 119245.

11 A. Wieckowska, E. Jablonowska, M. Dzwonek, M. Jaskolowski and R. J. C. Bilewicz, Tailored Lipid Monolayers Doped with Gold Nanoclusters: Surface Studies and Electrochemistry of Hybrid-film-covered Electrodes, *ChemElectroChem*, 2022, **9**(9), e202101367.

12 C. Li, Y. Guo, D. Tang, Y. Guo, G. Wang, H. Jiang and J. Li, Optimizing electron structure of Zn-doped $AgFeO_2$ with abundant oxygen vacancies to boost photocatalytic activity for Cr(VI) reduction and organic pollutants decomposition: DFT insights and experimental - ScienceDirect, *Chem. Eng. J.*, 2021, **411**, 128515.

13 T. Liu, C. Wang, M. Wang, J. Bai and Q. Zhou, The improved spatial charge separation and antibiotic removal performance on Z-scheme Zn-$Fe_2O_3/ZnIn_2S_4$ architectures, *Colloids Surf., A*, 2021, **628**, 127226.

14 S. Li, Y. Zhang and H. Huang, Black phosphorus-based heterostructures for photocatalysis and photoelectrochemical water splitting, *J. Energy Chem.*, 2022, **67**, 745–779.

15 Y. Jia, S. Li, H. Ma, J. Gao, G. Zhu, F. Zhang, J. Y. Park, S. Cha, J. S. Bae and C. Liu, Oxygen vacancy rich Bi_2O_4-Bi_4O_7-BiO_{2-x} composites for UV-vis-NIR activated high efficient photocatalytic degradation of bisphenol A, *J. Hazard. Mater.*, 2020, **382**(15), 121121.

16 M. Ghrib, T. Ghrib, W. Dimassi, M. Gaidi, R. Ouertani and H. Ezzaouia, Correlation between microstructural and optoelectronic properties of porous Si/SnO_2 composites coated Al_2O_3, *Optik*, 2022, **258**, 168900.

17 F. G. El Desouky, M. M. Saadeldin, M. A. Mahdy and I. K. El Zawawi, Tuning the structure, morphological variations, optical and magnetic properties of SnO2/NiFe2O4 nanocomposites for promising applications, *Vacuum*, 2021, **185**, 110003.

18 N. P. Reddy, R. Muniramaiah, R. Santhosh, J. M. Fernandes, D. B. Padmanaban, G. Maharana, M. Kovendhan, D. P. Joseph and B. Murali, Cost-effective Sb-doped SnO_2 films as stable and efficient alternative transparent

conducting electrodes for dye-sensitized solar cells, *J. Mater. Chem. C*, 2022, **20**, 7997–8008.

19 D. Liu, W. Zhang, Z. Ren and X. Li, Yb-doped SnO_2 electron transfer layer assisting the fabrication of high-efficiency and stable perovskite solar cells in air, *RSC Adv.*, 2022, **12**, 14631–14638.

20 P. Chen and Y. Wang, Improved arc erosion resistance of Ag/SnO_2 composites fabricated by Ag melt-infiltration in the SnO_2 skeleton, *Mater. Lett.*, 2022, **310**, 131520.

21 D. Maestre, E. Hernández, A. Cremades, M. Amati and J. Piqueras, Design, Synthesis and Characterization of Small Dimensional Structures of Er^{-} Doped SnO_2 and ErbiumTinOxide, *Cryst. Growth*, 2020, **12**(5), 2478–2484.

22 S. B. O. Dos Santos, M. H. Boratto, R. A. Ramos Jr and L. V. A. Scalvi, Influence of Pb^{2+} doping in the optical and electro-optical properties of SnO_2 thin films, *Mater. Chem. Phys.*, 2022, **278**, 125571.

23 L. Gnanasekaran, S. Rajendran, P. S. Kumar, A. K. Priya, F. Gracia, M. A. Habila and K. Saravanakumar, Visible light stimulated binary nanostructure and defect enriched TiO_2-SnO_2 for photocatalysis and antibacterial activity, *Mater. Lett.*, 2022, **316**, 131998.

24 L. Huang, J. Yao, L. Yang, J. Liu, J. Liu, S. Shu, M. Hua, Y. Song and H. Zhu, Compounds, Construction of Z-scheme $Bi_{12}O_{15}Cl_6/SnO_{2-x}$ heterojunction for enhanced photocatalytic degradation of dyes and antibiosis, *J. Alloys Compd.*, 2022, **908**, 164395.

25 W. Ren, J. Yang, J. Zhang, W. Li, C. Sun, H. Zhao, Y. Wen, O. Sha and B. Liang, Recent progress in SnO_2/g-C_3N_4 heterojunction photocatalysts: Synthesis, modification, and application, *J. Alloys Compd.*, 2022, **906**, 164372.

26 Z. Fan, J. Luan, C. Zhu and F. J. M. R. B. Liu, Depositing Ag_2S quantum dots as electron mediators in SnS_2/g-C_3N_4 nanosheet composites for constructing Z-scheme heterojunction with enhanced photocatalytic performance, *Mater. Res. Bull.*, 2021, **133**, 111045.

27 G. N. Silva, T. A. Martins, I. C. Nogueira, R. K. Santos, M. S. Li, E. Longo and G. Botelho, Synthesis of Ag_3PO_4/SnO_2 composite photocatalyst for improvements in photocatalytic activity under visible light, *Mater. Sci. Semicond. Process.*, 2021, **135**, 106064.

28 Y. Lian, Y. Wang, D. Zhang and L. Xu, Visible light-driven photocatalytic and enzyme-like properties of novel AgBr/Ag_2MoO_4 for degradation of pollutants and improved antibacterial application, *Colloids Surf., A*, 2022, **639**, 128348.

29 X. Hu, Q. Ma, X. Wang, Y. Yang, N. Liu, C. Zhang, N. Kawazoe, G. Chen and Y. Yang, Layered Ag/Ag_2O/$BiPO_4$/Bi_2WO_6 heterostructures by two-step method for enhanced photocatalysis, *J. Catal.*, 2020, **387**, 387.

30 B. Babu, R. Koutavarapu, V. V. N. Harish, J. Shim and K. Yoo, Novel in situ synthesis of Au/SnO_2 quantum dots for enhanced visible-light-driven photocatalytic applications, *Ceram. Int.*, 2019, **45**(5), 5743–5750.

31 M. A. Ahmed, A. Fahmy, M. G. Abuzaid and E. M. Hashem, Fabrication of novel $AgIO_4$/SnO_2 heterojunction for photocatalytic hydrogen production through direct Z-scheme mechanism, *J. Photochem. Photobiol., A*, 2020, **400**, 112660.

32 P. Wang, Y. Liu, N. Jiang, R. Jing and Y. Liu, Double S-scheme AgBr heterojunction co-modified with g-C_3N_4 and black phosphorus nanosheets greatly improves the photocatalytic activity and stability, *J. Mol. Liq.*, 2021, **329**, 115540.

33 S. Man, X. Zeng, Z. Yin, H. Yang, H. Bao, K. Xu, L. Wang, X. Ge, Z. Mo and W. J. E. A. Yang, Preparation of a novel Ce and Sb co-doped SnO_2 nanoflowers electrode by a two-step (hydrothermal and thermal decomposition) method for organic pollutants electrochemical degradation, *Electrochim. Acta*, 2022, **411**, 140066.

34 M. Herrera, D. Maestre, A. Cremades and J. Piqueras, Growth and Characterization of Mn Doped SnO_2 Nanowires, Nanobelts, and Microplates, *J. Phys. Chem. C*, 2020, **117**(17), 8997–9003.

35 Y. Zhang, Y. Zhao, Z. Xiong, T. Gao and J. Zhang, Elemental mercury removal by I-doped Bi_2WO_6 with remarkable visible-light-driven photocatalytic oxidation, *Appl. Catal., B*, 2021, **282**, 119534.

36 X. Feng, S. Zhang, F. Wang, J. Ma and X. Wang, Metallic Ag Confined on SnO_2 Surface for Soot Combustion: the Influence of Ag Distribution and Dispersion on the Reactivity, *ChemCatChem*, 2021, **13**(9), 2222–2233.

37 A. Mohammad, M. E. Khan, I. M. Alarifi, M. H. Cho and T. Yoon, A sensitive electrochemical detection of hydrazine based on SnO_2/CeO_2 nanostructured oxide, *Microchem. J.*, 2021, **171**, 106784.

38 J. Shin, J. N. Heo, J. Y. Do, Y. I. Kim and M. Kang, Effective charge separation in rGO/NiWO4@Au photocatalyst for efficient CO2 reduction under visible light, *J. Ind. Eng. Chem.*, 2019, **81**, 427–439.

39 T.-Y. Liang, S.-J. Chan, A. S. Patra, P.-L. Hsieh, Y.-A. Chen, H.-H. Ma and M. H. Huang, Inactive Cu_2O Cubes Become Highly Photocatalytically Active with Ag_2S Deposition, *ACS Appl. Mater. Interfaces*, 2021, **13**(9), 11515–11523.

40 X. Shen, J. Yang, T. Zheng, Q. Wang, H. Zhuang, R. Zheng, S. Shan and S. Li, Plasmonic p–n heterojunction of Ag/Ag_2S/Ag_2MoO_4 with enhanced Vis-NIR photocatalytic activity for purifying wastewater, *Sep. Purif. Technol.*, 2020, **251**, 117347.

41 B. Xue, H.-Y. Jiang, T. Sun, F. Mao, C.-C. Ma and J.-K. Wu, Microwave-assisted one-step rapid synthesis of ternary Ag/Ag2S/g-C_3N_4 heterojunction photocatalysts for improved visible-light induced photodegradation of organic pollutant, *J. Photochem. Photobiol., A*, 2018, **353**, 557–563.

42 X. Dong, S. Wang, Q. Wu, K. Liu, F. Kong and J. Liu, Co-catalyst boosted photocatalytic hydrogen production driven by visible-light over g-C_3N_4 : The synergistic effect between Ag and Ag_2S, *J. Alloys Compd.*, 2021, **875**, 160032.

43 H. Zhang, D. Yu, W. Wang, P. Gao and B. Liu, Construction of a novel BON-Br-AgBr heterojunction photocatalysts as a direct Z-scheme system for efficient visible photocatalytic activity, *Appl. Surf. Sci.*, 2019, **497**, 143820.

44 D. Liu, L. Feng, L. Cao, T. Xiao and J. Huang, W/O site replace by Ce/N of Bi_2WO_6 as cations/anions to regulate

the reduction potential of conduction band for enhanced photocatalytic degradation and hydrogen evolution capacity, *J. Alloys Compd.*, 2022, **890**, 161920.

45 H. Katsumata, M. A. I. Molla and J. B. Islam, Dual Z-scheme heterojunction g-C_3N_4/Ag_3PO_4/AgBr photocatalyst with enhanced visible-light photocatalytic activity, *Ceram. Int.*, 2022, **48**(15), 21898–21905.

46 Y. Li, M. Liu, M. Zhang, Y. Liu, Q. Zhao, X. Li, Q. Zhou, Y. Chen and S. Wang, Preparation of g-C_3N_4/TiO_2 Heterojunction Composite Photocatalyst by NaCl Template Method and Its Photocatalytic Performance Enhancement, *Nano*, 2023, **18**(02), 2350009.

47 J. Wang, G. Wang, B. Cheng, J. Yu and J. Fan, Sulfur-doped g-C_3N_4/TiO_2 S-scheme heterojunction photocatalyst for Congo Red photodegradation, *Chin. J. Catal.*, 2021, **42**(1), 56–68.

48 X. Guo, H. Wang, L. Wang, D. Zeng and Q. Xiang, Triple-Mode Bi_2WO_6/Pg-C_3N_4@rGO Core-Shell Synergistic Effect with Enhanced Light-induced Photocatalytic Activity, *Bull. Korean Chem. Soc.*, 2019, **40**(3), 254–261.

49 P. Bai, N. Wu, Y. Wang, T. Yang and X. Wang, PH-controllable Regeneration and Visible-light Photocatalytic Redox of Carbon and Nitrogen Codoped $Zn_3Nb_2O_8$ towards Multiple Contaminants, *Catal. Sci. Technol.*, 2020, **10**(9), 2810–2820.

50 A. Q. Alorabi, Effective Removal of Malachite Green from Aqueous Solutions Using Magnetic Nanocomposite: Synthesis, Characterization, and Equilibrium Study, *Adsorpt. Sci. Technol.*, 2021, **2021**, 2359110.

51 P. Wang, Y. Cao, X. Zhou, C. Xu and Q. Yan, Facile construction of 3D hierarchical flake ball-shaped γ-AgI/Bi_2WO_6 Z-scheme heterojunction towards enhanced visible-light photocatalytic performance - ScienceDirect, *Appl. Surf. Sci.*, 2020, **531**, 147345.

52 M. K. A. Mohammed, Lithium-doped SnO_2@CeO_2nanoparticles for highly photodegradation of Rhodamine B dye upon visible light irradiation, *Int. J. Mod. Phys. B*, 2023, **37**(04), 2350036.

53 N. K. Razdan and A. Bhan, Catalytic site ensembles: A context to reexamine the Langmuir-Hinshelwood kinetic description, *J. Catal.*, 2021, **404**, 726–744.

54 C. Han, L. Ge, C. Chen, Y. Li, X. Xiao, Y. Zhang and L. Guo, Novel visible light induced Co_3O_4-g-C_3N_4 heterojunction photocatalysts for efficient degradation of methyl orange, *Appl. Catal., B*, 2014, **147**, 546–553.

55 M. May-Lozano, R. Lopez-Medina, V. Mendoza-Escamilla, G. Rivadeneyra-Romero and S. Martínez-Delgadillo, Intensification of the Orange II and Black 5 degradation by sonophotocatalysis using Ag-graphene oxide/TiO_2 systems, *Chem. Eng. Process.*, 2020, **158**, 108175.

56 Y. Song, J. Qi, J. Tian, S. Gao and F. Cui, Construction of Ag/g-C_3N_4 photocatalysts with visible-light photocatalytic activity for sulfamethoxazole degradation, *Chem. Eng. J.*, 2018, **341**, 547–555.

57 X. Lei, M. You, F. Pan, M. Liu, P. Yang, D. Xia, Q. Li, Y. Wang and J. Fu, $CuFe_2O_4$@GO nanocomposite as an effective and recoverable catalyst of peroxymonosulfate activation for degradation of aqueous dye pollutants, *Chin. Chem. Lett.*, 2019, **30**(12), 245–249.

58 Y. Shaveisi and S. Sharifnia, Deriving Ag_3PO_4–CaO composite as a stable and solar light photocatalyst for efficient ammonia degradation from wastewater, *J. Energy Chem.*, 2018, **27**(01), 304–313.

59 Y. Yang, X. Hu, Y. Zhao, L. Cui, Z. Huang, J. Long, J. Xu, J. Deng, C. Wu and W. Liao, Decontamination of tetracycline by thiourea-dioxide-reduced magnetic graphene oxide: Effects of pH, ionic strength, and humic acid concentration, *J. Colloid Interface Sci.*, 2017, **495**, 68–77.

60 A. Yqg, B. Nyg, B. Whc, B. Yfz, Z. A. Jia and B. Dqy, UV-activated persulfate oxidation of sulfamethoxypyridazine: Kinetics, degradation pathways and impact on DBP formation during subsequent chlorination, *Chem. Eng. J.*, 2019, **370**, 706–715.

61 J. Niu, Y. Li and W. Wang, Light-source-dependent role of nitrate and humic acid in tetracycline photolysis: Kinetics and mechanism, *Chemosphere*, 2013, **92**(11), 1423–1429.

62 R. Cheng, M. Kang, Z. Shen, L. Shi and X. Zheng, Visible-light-driven photocatalytic inactivation of bacteriophage f2 by Cu-TiO_2 nanofibers in the presence of humic acid, *J. Environ. Sci.*, 2019, **77**, 383–391.

63 T. Tang, G. Lu, W. Wang, R. Wang, K. Huang, Z. Qiu, X. Tao and Z. Dang, Photocatalytic removal of organic phosphate esters by TiO_2: Effect of inorganic ions and humic acid, *Chemosphere*, 2018, **206**, 26–32.

64 A. Cai, J. Deng, M. Xu, T. Zhu, S. Zhou, J. Li, G. Wang and X. Li, Degradation of tetracycline by UV activated monochloramine process: Kinetics, degradation pathway, DBPs formation and toxicity assessment, *Chem. Eng. J.*, 2020, **395**, 125090.

65 Z. Hassan, Effects of pH on Antibiotic Denitrification and Biodegradation of Sulfamethoxazole Removal from Simulated Municipal Wastewater by a Novel 3D-BER System, *J. Environ. Eng.*, 2020, **146**(12), 04020134.

66 Q. Chen, B. He, Y. Ma, X. Wang, Q. Xiong, J. Li and Q. H. J. P. P. Liu, Polymers, Influence of the pH value on the degradation of an azo dye of methyl orange by air discharge plasma, *Plasma Processes Polym.*, 2019, **16**(5), 1800152.

67 M. F. Hanafi and N. Sapawe, Influence of pH on the photocatalytic degradation of methyl orange using nickel catalyst, *Mater. Today: Proc.*, 2020, **31**, 339–341.

68 Y. Chen, Y. Zhang, C. Liu, A. Lu and W. Zhang, Photodegradation of Malachite Green by Nanostructured Bi WO Visible Light-Induced Photocatalyst, *Int. J. Photoenergy*, 2011, **2012**(1), 1302–1312.

69 W. Li, M. Xu, Q. Cao, J. Luo, S. Yang and G. Zhao, Magnetic GO/Fe_3O_4 for rapid malachite green (MG) removal from aqueous solutions: a reversible adsorption, *RSC Adv.*, 2021, **11**, 19387–19394.

70 E. Sharifpour, E. A. Dil, A. Asfaram, M. Ghaedi and A. Goudarzi, Optimizing adsorptive removal of malachite green and methyl orange dyes from simulated wastewater by Mn-doped CuO-Nanoparticles loaded on activated carbon using CCD-RSM: Mechanism, regeneration,

isotherm, kinetic, and thermodynamic studies, *Appl. Organomet. Chem.*, 2019, **33**(3), e4678.

71 A.-T. Vu, V. H. Mac, T. H. Nguyen and T. H. Nguyen, Preparation of carnation-like Ag-ZnO composites for enhanced photocatalysis under visible light, *Nanotechnology*, 2023, **34**(27), 275602.

72 B. Prakash, V. Katoch, A. Shah, M. Sharma and A. K. Ganguli, Continuous Flow Reactor for The Controlled Synthesis and Inline Photocatalysis of Antibacterial Ag_2S Nanoparticles, *Photochem. Photobiol.*, 2020, **96**(6), 1273–1282.

73 P. P. Tun, J. Wang, T. T. Khaing, X. Wu and G. Zhang, Fabrication of functionalized plasmonic Ag loaded Bi_2O_3/montmorillonite nanocomposites for efficient photocatalytic removal of antibiotics and organic dyes, *J. Alloys Compd.*, 2019, **818**, 152836.

74 G. Yentür and M. Dükkancı, Fabrication of magnetically separable plasmonic composite photocatalyst of Ag/AgBr/$ZnFe_2O_4$ for visible light photocatalytic oxidation of carbamazepine, *Appl. Surf. Sci.*, 2020, **510**, 145374.

75 A. Rezaei, M. R. Rezaei and M. H. Sayadi, 3D network structure graphene hydrogel-Fe3O4@SnO_2/Ag *via* an adsorption/photocatalysis synergy for removal of 2,4 dichlorophenol, *J. Taiwan Inst. Chem. Eng.*, 2021, **121**, 154–167.

76 J. Lan, B. He, C. Haw, M. Gao and J. Kang, Band Engineering of ZnO/Si Nanowire Arrays in Z-Scheme Heterojunction for Efficient Dye Photodegradation, *Appl. Surf. Sci.*, 2020, **529**, 147023.

77 Y. Xue, W. Tang, H. Gu, M. Wei, E. Guo, Q. Lu and Y. Pang, Flexible Bi_2MoO_6/N-doped carbon nanofiber membrane enables tetracycline photocatalysis for environmentally safe growth of Vigna radiata, *J. Alloys Compd.*, 2022, **902**, 163860.

78 H. Shen, X. Zhao, L. Duan, R. Liu and H. Li, Enhanced visible light photocatalytic activity in SnO2@g-C3N4 core-shell structures, *Mater. Sci. Eng., B*, 2017, **218**, 23–30.

79 S. Zarezadeh, A. Habibi-Yangjeh and M. Mousavi, BiOBr and AgBr co-modified ZnO photocatalyst: A novel nanocomposite with p-n-n heterojunctions for highly effective photocatalytic removal of organic contaminants, *J. Photochem. Photobiol., A*, 2019, **379**, 11–23.

80 M. Ge and Z. Li, All-Solid-State Z-Scheme Photocatalytic Systems Based on Silver-Containing Semiconductor Materials, *Prog. Chem.*, 2017, **29**(8), 846–858.

81 H. Guo, C. G. Niu, L. Zhang, X. J. Wen, C. Liang, X. G. Zhang, D. L. Guan, N. Tang and G. Zeng, Engineering, Construction of direct Z-scheme AgI/$Bi_2Sn_2O_7$ nanojunction system with enhanced photocatalytic activity: Accelerated interfacial charge transfer induced efficient Cr(VI) reduction, tetracycline degradation and Escherichia coli inactivation, *ACS Sustainable Chem.*, 2018, **6**(6), 8003–8018.

82 R. Xie, L. Zhang, H. Xu, Y. Zhong, X. Sui and Z. Mao, Fabrication of Z-scheme photocatalyst Ag-AgBr@$B_{i20}TiO_{32}$ and its visible-light photocatalytic activity for the degradation of isoproturon herbicide, *J. Mol. Catal. A: Chem.*, 2015, **406**, 194–203.

83 X. Wang, S. Li, Y. Ma, H. Yu and J. Yu, H2WO4 center dot H_2O/Ag/AgCl Composite Nanoplates: A Plasmonic Z-Scheme Visible-Light Photocatalyst, *J. Phys. Chem. C*, 2011, **115**(30), 14648–14655.

84 L. V. Trandafilović, D. J. Jovanović, X. Zhang, S. Ptasińska and M. D. Dramićanin, Enhanced photocatalytic degradation of methylene blue and methyl orange by ZnO:Eu nanoparticles, *Appl. Catal., B*, 2017, **203**, 740–752.

85 A. Barapatre, K. R. Aadil and H. Jha, Biodegradation of Malachite Green by the Ligninolytic Fungus Aspergillus flavus, *Clean: Soil, Air, Water*, 2017, **45**(4), 1600045.

86 J. Kaur and S. Singhal, Facile synthesis of ZnO and transition metal doped ZnO nanoparticles for the photocatalytic degradation of Methyl Orange, *Ceram. Int.*, 2014, **40**(5), 7417–7424.

87 A. Bahramian, M. Rezaeivala, K. He and D. D. Dionysiou, Enhanced visible-light photoelectrochemical hydrogen evolution through degradation of methyl orange in a cell based on coral-like Pt-deposited TiO_2 thin film with sub-2 nm pores, *Catal. Today*, 2019, **335**, 333–344.

88 B. P. Sanjay, S. Sandeep, A. S. Santhosh, C. S. Karthik, D. N. Varun, N. K. Swamy, P. Mallu, K. S. Nithin, R. J. Ramalingam and K. Muthusamy, Unprecedented 2D GNR-CoB nanocomposite for detection and degradation of malachite green – A computational prediction of degradation pathway and toxicity, *Chemosphere*, 2022, **287**, 132153.